Chemical Science

ROYAL SOCIETY OF CHEMISTRY

EDGE ARTICLE

View Article Online
View Journal | View Issue

Cite this: *Chem. Sci.*, 2025, **16**, 17725

All publication charges for this article have been paid for by the Royal Society of Chemistry

Hierarchical hollow nanospheres of imine-based covalent organic frameworks with built-in Ag sites for fast-charging lithium metal batteries

Tiancun Liu, †*[a] Xiao-Meng Lu,†[b] Song Lu, [a] Ronghan Jiang,[a] Min Guo,[a] Chaofei Guo, *[c] Zhixin Yu [d] and Yong Wang *[b]

Received 20th May 2025
Accepted 25th August 2025

DOI: 10.1039/d5sc03645c

rsc.li/chemical-science

Lithium metal is deemed to be the ultimate anode material for high-energy-density and fast-charging lithium batteries. However, issues of dendritic deposition and frangible solid electrolyte interphases must be resolved for lithium metal anodes. Herein, a hybrid interfacial layer, hierarchical hollow nanospheres assembled from lithiophilic imine-based covalent organic frameworks and built-in Ag sites (Ag@ICOFs), has been applied to regulate the interfacial lithium ion flux and enhance the anode stability for effectively inhibiting dendrite formation. The hollow ICOFs play important roles in enhancing electrolyte infiltration caused by ordered porous channels and promoting uniform lithium distribution due to the superior lithiophilic ability of binding sites (C=N groups and benzene rings). Moreover, the filling of Ag can induce internal deposition in hollow Ag@ICOFs nanospheres when lithium metal tends to grow vertically. The dendrite-free lithium development is further verified by *in situ* electrochemical electrode measurements and theoretical calculation. As a result, a synergistic enhancement in electrochemical performance is realized through stable long-term 1000 cycles and excellent capacity retention (87.3%) at a quick charge/discharge of 5C in a full cell paired with a $LiFePO_4$ cathode. This work provides a fresh exploration of constructing functional nanomaterials with hierarchical structures for energy storage.

Introduction

Lithium metal batteries (LMBs) boast an ultra-high theoretical capacity of 3860 mAh g^{-1}, a relatively low mass density of 0.534 g cm^{-3}, and a low electrode potential of −3.04 V *versus* the standard hydrogen electrode and are therefore widely recognized as some of the most promising rechargeable energy storage devices.[1,2] However, the efficiency and lifespan of LMBs are substantially depressed due to side reactions between the highly active lithium metal and the electrolyte and the growth of lithium dendrites during successive lithium plating/stripping processes.[3–10] To make matters worse, these dendrites can eventually penetrate the separator, which can cause serious safety issues if these side effects turn more fatal.[11] Many studies have been conducted to solve the aforementioned problems, including building multi-dimension frameworks,[12–15] optimizing electrolyte recipes,[16–18] and inventing functional separators.[3,19] It is a feasible approach to architect an artificial solid-state electrolyte interphase (ASEI) on the surface of lithium metal to achieve synergistic benefits such as rapid lithium ion transport, electrolyte-lithium isolation, and prevention of lithium dendrite growth and electrode volume expansion to boost the properties of LMBs.[20] Currently, inorganic-dominated ASEIs have been broadly employed to modulate lithium–metal interfacial properties, including Li alloys,[21,22] metal oxides,[23,24] carbon-based materials,[25–27] and so on. Lithiophilic metal decoration tends to guide planar Li deposition and development on electrode interfaces.[28,29] In particular, the Ag component shows superior lithiophilicity and better improvement capability in achieving dendrite-free lithium growth.[30–32] Unlike inorganic-dominated ASEIs, organic polymers provide functional and structural flexibility to optimally tune lithium-ion migration and mechanical strength, thereby inhibiting the growth of lithium dendrites.

Significantly, covalent organic frameworks (COFs) and their derivatives, with their constant porosity, well-defined nanochannels, and functional backbones, have greatly motivated the fabrication of ionic "sieve plates".[33–35] Due to the high mechanical modulus, COF decoration layers play a role in suppressing the tip growth of deposited Li.[36,37] Moreover, relying on their molecular design versatility, well-defined one-

[a]*Institute of New Energy, School of Chemistry and Chemical Engineering, Shaoxing University, Shaoxing 312000, Zhejiang, China. E-mail: liutc@usx.edu.cn*

[b]*Department of Chemical Engineering, School of Environmental and Chemical Engineering, Shanghai University, 99 Shangda Road, Shanghai 200444, China. E-mail: yongwang@shu.edu.cn*

[c]*Zhejiang Provincial Key Laboratory of Chemical Utilization of Forestry Biomass, Department of Chemistry, Zhejiang A&F University, Hangzhou 311300, China. E-mail: chaoguo@zafu.edu.cn*

[d]*Department of Energy and Petroleum Engineering, University of Stavanger, 4036 Stavanger, Norway*

† Co-author.

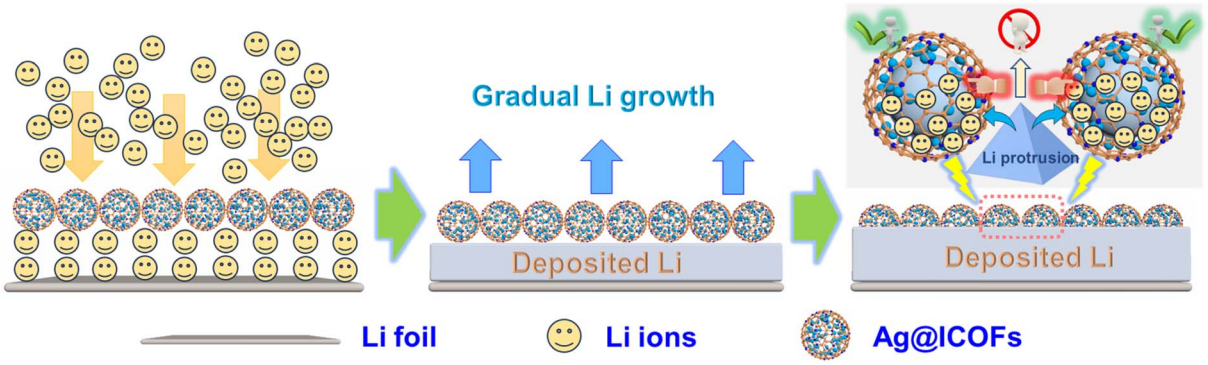

Scheme 1 Lithium deposition evolution on Li foil decorated with Ag@ICOFs.

dimensional channels, and formidable physicochemical stability, layered 2D COFs are endowed with the ability to facilitate uniform lithium transport, adjust lithium deposition, and suppress dendrite formation in ASEI films.[38,39] However, the most commonly implemented COF electrodes have a two-dimensional structure and a tightly stacked morphology, which would inadequately expose the active sites and impede the Li^+ transport performance.[40] Furthermore, managing the growth of COFs by template methods to fulfill the unusual hollow spherical forms has been evidenced as another effective method to obtain stable structures and homogeneous morphologies of COFs, but only a few investigations have been conducted on it so far. Regrettably, enhanced hybrid SEIs combining inorganic lithium alloys and organic hollow spherical covalent organic frameworks have not been reported to date.

Differing from these studies, mainly focusing on the optimization of dendrite formation in the initial stage and ignoring the dendrite issue once the vertical Li tendency occurs, in this work, a hybrid interfacial layer, lithiophilic hollow nanospheres assembled from imine-based covalent organic framework (ICOF) layers and built-in Ag sites (Ag@ICOFs), is constructed and proved to be capable of guiding dendrite-free lithium deposition (Scheme 1). On the one hand, hollow ICOF nanospheres actualize enough exposure of lithiophilic functional groups such as C=N linkages and aromatic rings, which can bind lithium ions and promote uniform distribution on the electrode surface, effectively avoiding the locally concentrated lithium growth. On the other hand, the internal decoration of Ag nanoseeds helps improve the conductivity, achieving rapid electron migration in Ag@ICOFs. More importantly, once deposited, lithium shows protrusion development, and lithiophilic Ag can guide directional nucleation and break vertical growth, further alleviating the dendrite formation. By conducting *in/ex situ* measurements, the superior capabilities of guiding homogenous and flat Li deposition and reducing the side reaction of electrolyte loss have been proved, positively verifying the rational protection design for lithium metal anodes. Depending on these positive effects, the Ag@ICOFs covered electrode exhibits an improved coulombic efficiency (CE) of 99.4% for 400 cycles and a long lifespan of 1900 h for a symmetric cell at 0.5 mA cm^{-2}. Moreover, the full cells comprising Ag@ICOFs covered lithium anodes and $LiFePO_4$ cathodes can obtain an ultrahigh capacity of 101.8 mAh g^{-1} (capacity retention ratio: 87.3%) after 1000 cycles at 5C. This work offers a promising insight into the exploitation of novel composite ASEI layers.

Results and discussion

The brief fabrication process and optical photographs of the corresponding powders for producing various materials are shown in Fig. 1. Specifically, mesoporous silica dioxide (SiO_2) spheres are synthesized by the solvothermal method and then used as the initial template. Meanwhile, $AgNO_3$ is also selected as the precursor for preparing Ag nanoseeds by mild-temperature chemical reduction. Compared to other metals, Ag decoration not only exhibits excellent lithiophilicity in inducing Li deposition, but also helps promote rapid electron migration in Ag@ICOFs because of its better conductivity. Afterwards, it is necessary to decorate the amino group on the SiO_2@Ag surface for promoting the subsequent amino-aldehyde condensation and enhancing decoration uniformity. Therefore, the outside growth of imine-based covalent organic frameworks (ICOFs) can be achieved by adding *p*-phthalaldehyde (TA) and a 1,3,5-tris(4-aminophenyl)benzene (TAPB) monomer. At last, the diluted NaOH solution (1 M) is employed to remove the SiO_2 template during the fabrication of hollow Ag@ICOFs. In particular, the sample has changed from white to yellow after the functional decoration of ICOFs, further indicating the preparation of Ag@ICOFs.

Fig. 2a–c show scanning electron microscopy (SEM) images of SiO_2, SiO_2@Ag@ICOFs and hollow Ag@ICOFs samples, from which the spherical morphology and uniform sizes of ~600 nm in diameter can be well maintained despite the addition of Ag nanoseeds and ICOF growth. Moreover, as displayed in related transmission electron microscopy (TEM) images (Fig. 2d–g), SiO_2 with a single structure, core–shell SiO_2@Ag@ICOFs and hollow Ag@ICOFs have been successfully constructed. Specifically, due to the necessary consumption of amino groups binding with Ag, the additional amino decoration on SiO_2 nanospheres could be beneficial for improving the amino-aldehyde condensation (Fig. S1). For as-prepared

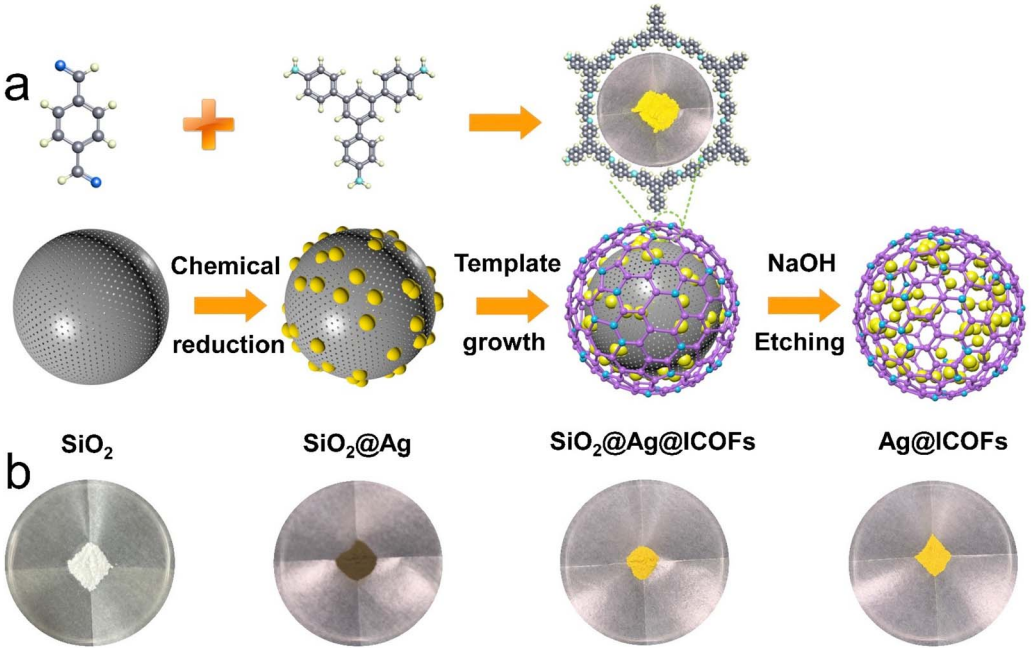

Fig. 1 (a) Schematic illustration of the synthesis route for Ag@ICOFs. (b) Optical photographs of products at various stages.

SiO_2@Ag@ICOFs, layer-assembled ICOFs were produced and small Ag nanoparticles were distributed on the outer walls of SiO_2 and within the ICOF layer. Notably, accumulated Ag nanoparticles have been changed into dispersed nanoseeds after removing the SiO_2 template in Ag@ICOFs, which may be caused by weak binding between particles. Dispersed Ag sites can definitely promote more nucleation sites for lithium metal. Moreover, abundant void space can alleviate the volume expansion. As presented in the HRTEM image of Ag nanoseeds (Fig. 2h), the planar spacing of the subject lattice stripes is 0.23 nm, which corresponds to the (111) plane of the face-centered cubic Ag. The dark-field scanning TEM images of the Ag@ICOFs composite reveal that granular Ag is randomly dispersed inside ICOFs without agglomeration (Fig. 2i). The EDS spectra of Ag@ICOFs (Fig. 2j–l) also illustrate the even distribution of C, N and Ag elements in the void structure.

The powder X-ray diffraction (PXRD) patterns of SiO_2@Ag, pristine ICOFs and the Ag@ICOFs material are shown in Fig. 3a. The related PXRD patterns of ICOFs and Ag@ICOFS show an evident intense diffraction peak at ~3.0°, which is clearly related to the (100) crystalline plane of the ICOF structure and consistent with other studies.[41] Specifically, two further diffraction peaks at 38.2° (corresponding to the (111) plane) and 44.4° (corresponding to the (200) plane) that are attributed to the face-centered cubic Ag (JCPDS card no. 4-783) are discovered after the modification of Ag nanoparticles.[42] Furthermore, the Fourier-transform infrared spectroscopy (FT-IR, Fig. 3b) results manifest that the specific peaks attributed to the C=N bond (1618 cm^{-1}) are discernible for Ag@ICOFs. Besides, the unreacted sites of aldehyde (–HC=O) and amino ($-NH_2$) groups at the borders of the ICOF layered structure can be attributed to the tiny peaks at approximately 1696 and 3365 cm^{-1}.[43] In addition, Ag@ICOFs products can maintain good thermal stability up to 450 °C which can be verified from the thermogravimetric analysis (TGA, Fig. 3c) results. Furthermore, the weight ratio of Ag sites in Ag@ICOFs was determined at approximately 38.2 wt% after complete decomposition at 800 °C under air conditions, indicating that moderate Ag loading is necessary, which meets the demand for inducing the dispersed and internal nucleation of plated Li. The nitrogen adsorption–desorption isotherm reveals that Ag@ICOFs (Fig. 3d) has a mesoporous structure with a BET surface area of 289.5 m^2 g^{-1}. The deviation between the adsorption and desorption isotherms, especially in the low relative pressure region, is caused by hysteresis behavior, which is a common phenomenon observed in nitrogen sorption measurements for COF materials.[44,45] A larger BJH pore size of 2.6 nm can promote the diffusion of Li ions (Fig. S2). X-ray photoelectron spectroscopy (XPS) characterization was further performed to reveal the detailed composition and elemental states of Ag@ICOFs. As shown in Fig. 3e, C, N and Ag elements can be clearly detected in the hollow Ag@ICOFs material. Peaks at 286.5, 285.2, 284.3 and 283.4 eV in the high-resolution C 1s spectra are attributed to C–N, C–C, C=C and C=N, respectively (Fig. 3f).[46–49] The high-resolution N 1s spectrum (Fig. 3g) displays two nitrogen species: N–C and N=C at 400.6 and 399.2 eV, respectively.[50–52] Two distinct peaks at 374.8 and 368.3 eV, corresponding to Ag $3d_{3/2}$ and Ag $3d_{5/2}$, are visible in the Ag 3d spectrum of Ag@ICOFs (Fig. 3h).[53,54] As a result, the functional Ag@ICOFs materials with multi-lithiophilic groups have been reasonably and successfully prepared. Moreover, the contact angles of an ether-based electrolyte (1 M LiTFSI dissolved in DOL/DME (1 : 1, v/v) and 0.2 M $LiNO_3$) with ICOFs and Ag@ICOFs layers were

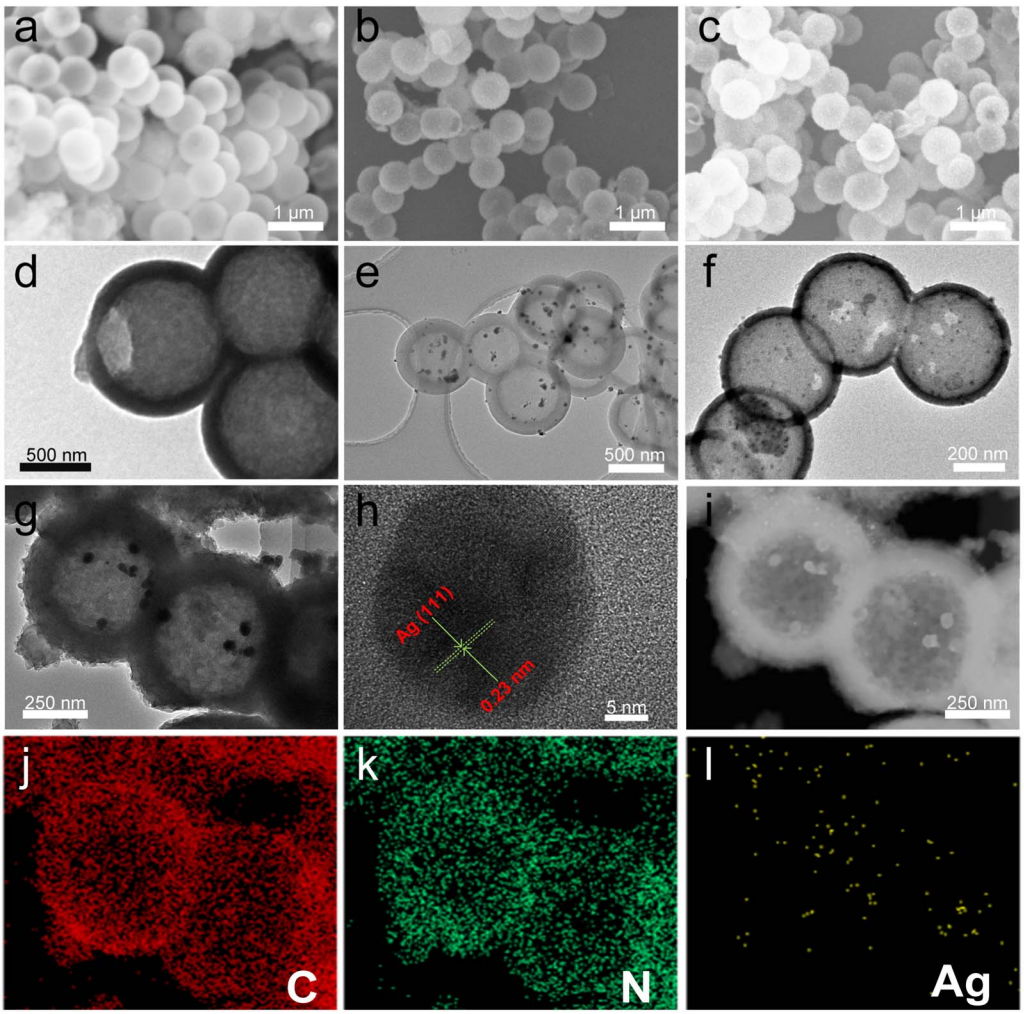

Fig. 2 SEM images of (a) SiO_2, (b) SiO_2@Ag@ICOFs and (c) Ag@ICOFs. TEM images of (d) SiO_2, (e) SiO_2@Ag and (f and g) Ag@ICOFs. (h) High-resolution TEM image displaying lattice fringes of the Ag nanoparticles. (i) Three-dimensional image. Dark-field scanning TEM image of Ag@ICOFs. (j–l) Elemental mapping images of C, N, and Ag in Ag@ICOFs.

measured, which can be observed in Fig. 3i. The contact angle of Ag@ICOFs is determined to be 25.6°, which is slightly smaller than that of ICOFs (51.4°), implying that the Ag@ICOFs layer shows better electrolyte wettability. Therefore, more dispersed distribution of Li^+ flux and Li deposition on the electrode surface will be favored.

To examine the impact of Ag@ICOFs on Li deposition, a galvanostatic discharge test was conducted at 0.5 mA cm^{-2} in asymmetric cells that contained Li foil and either pristine Cu or ICOFs and an Ag@ICOFs covered Cu electrode. As demonstrated in Fig. 4a, S3 and S4, a low nucleation overpotential of 9.6 mV is exhibited by Ag@ICOFs, which is smaller than those of ICOFs (25.2 mV) and bare Cu (47.0 mV), demonstrating the improved lithiophilicity of Ag and ICOF decoration. SEM images were also obtained to explore the morphology change in the Ag@ICOFs covered electrode deposited with different capacities of Li metal. Specifically, Ag@ICOFs can still maintain a smooth surface at a plating time of 2 h, similar to the pristine conditions (Fig. 4b). Afterwards, observable voids are gradually filled with Li as Li plating time increases to 6 h, obviously indicating the inducing effect provided by lithiophilic sites (Fig. 4c). Fig. 4d shows uniform Li growth and a non-dendritic situation in Ag@ICOFs as loading capacity reaches 5 mAh cm^{-2}. Nevertheless, after Li plating for 6 h and 10 h, metallic Li would be coarsely deposited on the bare Cu surface (Fig. S5a), and continuous Li deposition encountered dendritic development that may increase the risk of short circuit (Fig. S5b). It can be assumed that hierarchical lithiophilic sites in Ag@ICOFs, including exposed C=N groups, benzene rings, and internal Ag nanoparticles, play a crucial role in homogenizing the interfacial Li ion flux and guiding directional lithium deposition. The abundant lithiophilic sites in the ICOF framework first facilitate the dispersion of Li ions, preventing local concentration and promoting uniform Li distribution on the electrode surface. More importantly, when lithium tends to form protrusions, the lithiophilic Ag sites guide directional nucleation and inhibit vertical growth, thereby preventing dendrite formation. This combined action of the ICOFs and Ag nanoparticles contributes

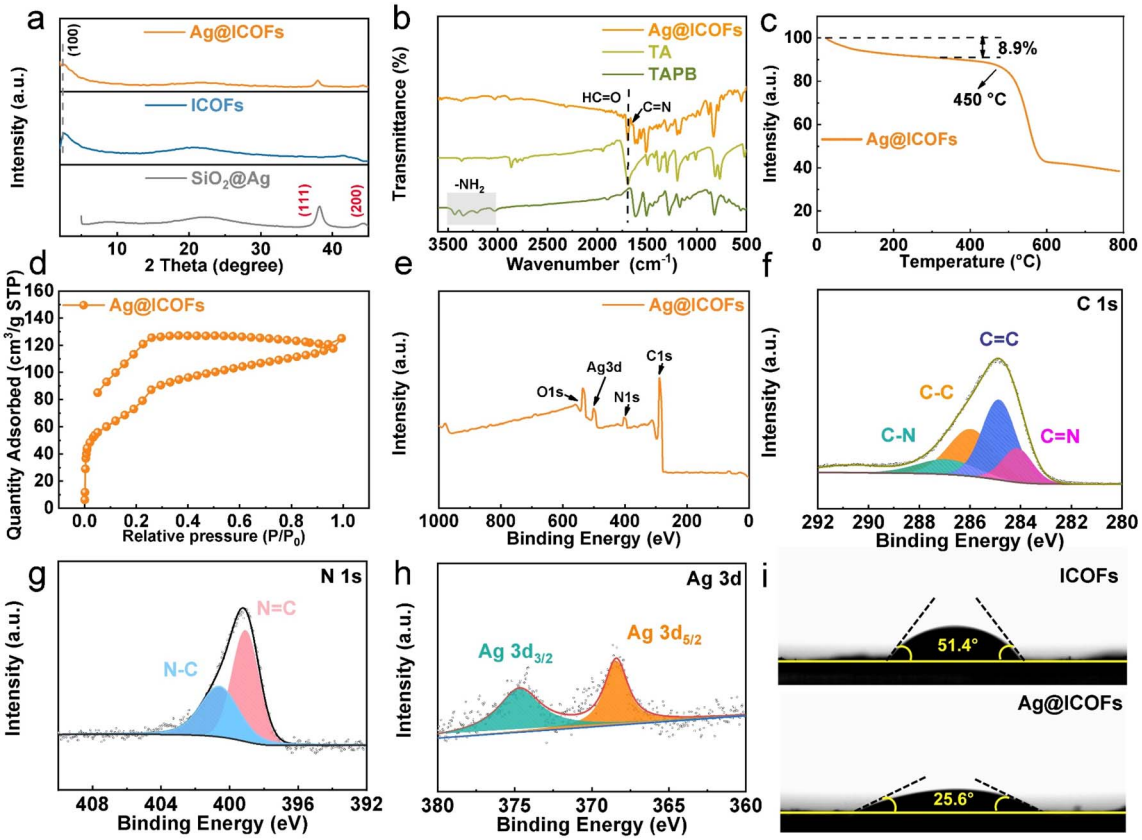

Fig. 3 (a) XRD patterns of SiO_2@Ag, ICOFS, and Ag@ICOFs. (b) FT-IR spectra of Ag@ICOFs. (c) TGA analyses of Ag@ICOFs in the air. (d) Nitrogen adsorption–desorption isotherms of Ag@ICOFs. (e) XPS full patterns of Ag@ICOFs. High-resolution (f) C 1s, (g) N 1s and (h) Ag 3d XPS spectra. (i) Contact angle measurement of ICOFs and Ag@ICOFs.

to the uniform deposition and enhanced stability of the lithium metal anode.

An *in situ* optical micrograph test was also performed to observe the evolution of Li deposition on the electrode using the Ag@ICOFs layer. As shown in Fig. 4e–g, the Li metal electrode equipped with Ag@ICOFs achieves a relatively smooth surface morphology without any dendrites during the plating process, which is consistent with the aforementioned SEM observation. In contrast, the cross-sectional images of two symmetric cells with bare Li and Li@ICOFs, which were subjected to the same current density of 1 mA cm^{-2} at different time intervals, reveal that the surfaces of the two electrodes were smooth in their initial state (Fig. S6). However, dendrite formation could be observed after Li plating for 1 h, followed by the appearance of some mossy dendrites on the surface. On extending the plating time (beyond 60 minutes), more observable dendrites appeared, potentially causing short circuits from several large dendrites and presenting substantial safety hazards for LMBs. As exhibited in Fig. S7–S9, theoretical calculation was conducted to better explore the observable difference of Li plating on various substrates. In particular, more intensive electron accumulation can be noticed at C=N groups and benzene rings, promoting the preferential attraction and dispersed distribution of Li ions. Moreover, the obtained results about adsorption energy of lithiophilic sites with Li ions further demonstrate the superior directional inducement of ICOFs, from which high adsorption energies of −1.53 and −1.45 eV can be obtained by the C=N group and benzene ring respectively. Subsequently, compared to pristine ICOFs, the reduced band gap is shown by Ag@ICOFs (Fig. S9), thereby modulating the electron distribution on the surface, which is definitely beneficial for facilitating more homogeneous and rapid Li^+ transference.

Fig. 4h illustrates the positive synergistic effect of hollow Ag@ICOFs loaded dual-lithiophilic sites, inorganic Ag and organic outer layers, in circumventing the critical problem of dendritic growth. On the one hand, the ordered and regular channels and lithiophilic groups (C=N groups and benzene rings) can guide the initially homogeneous distribution of immigrated Li ions on the electrode surface, reduce the nucleation barrier, and then promote stable deposition and growth. On the other hand, built-in Ag nanoseeds can adjust the direction by attracting Li ions and then guiding internal deposition when Li growth encounters the vertical development. In sharp contrast, uneven ion dispersion on the electrode interface will cause locally concentrated Li nucleation and uncontrollable evolution, thereby inducing fatal dendrite generation and increasing the safety risk (Fig. 4i).

Coulombic efficiency (CE) is a crucial indicator for exploring the plating and stripping behaviors, which is determined by the capacity ratio of Li stripping to plating in each cycle.[55] As shown

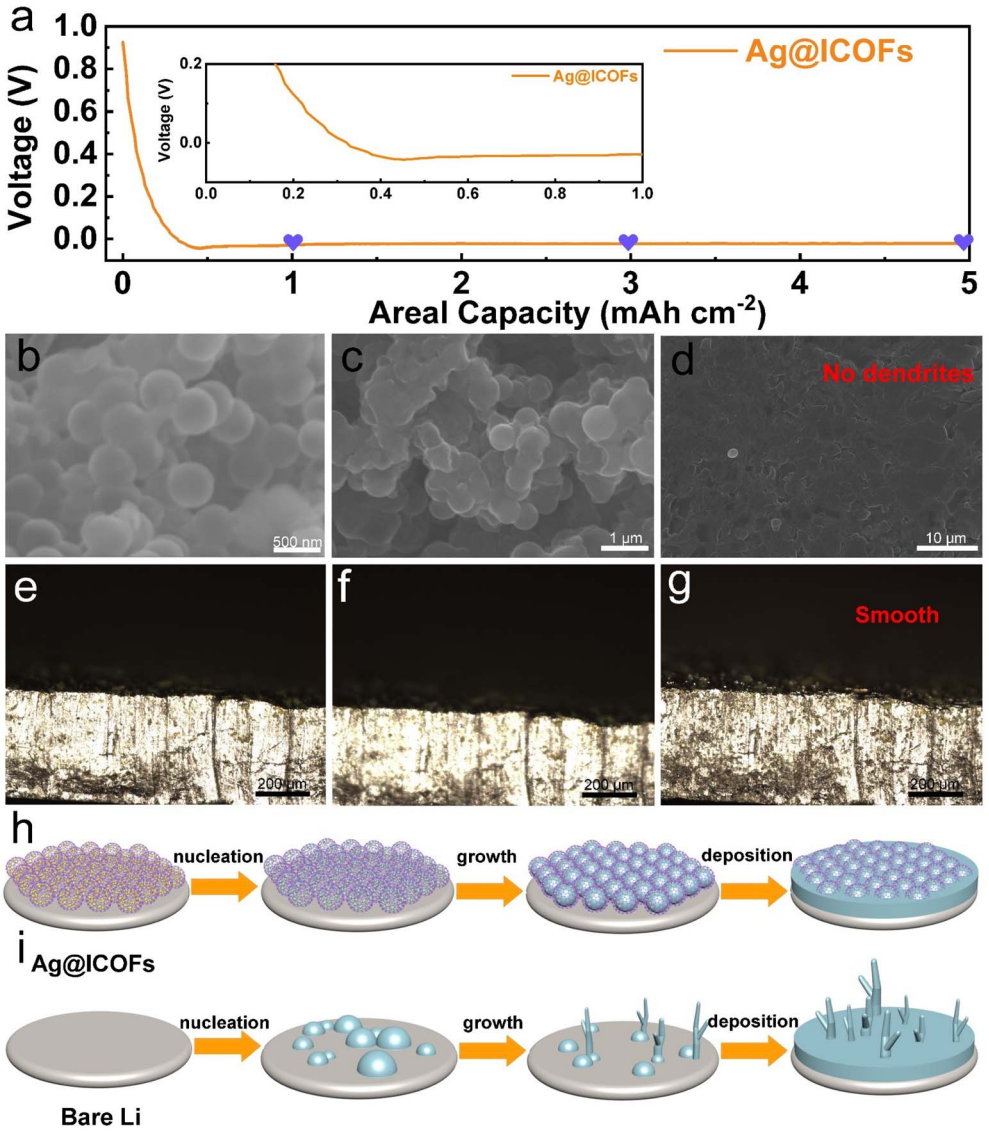

Fig. 4 (a) Initial voltage–capacity profiles of Ag@ICOFs cells at a current density of 0.5 mA cm^{-2}. Top-view SEM images of the Ag@ICOFs electrode after being plated with (b) 1 mAh cm^{-2}, (c) 3 mAh cm^{-2}, and (d) 5 mAh cm^{-2} of Li. The corresponding *in situ* optical microscopy observations of the Li-deposition process on Ag@ICOFs for (e) 1 mAh cm^{-2}, (f) 3 mAh cm^{-2} and (g) 5 mAh cm^{-2}. A diagram of Li plating in (h) Ag@ICOFs and (i) bare Li at various states.

in Fig. 5a, the electrode with Ag@ICOFs exhibits a highly stable and exceptionally high CE value of 98.8% over 430 cycles at 0.5 mA cm^{-2}. This performance is significantly better than that of the ICOF decorated electrode (147 cycles). As demonstrated in Fig. 5b, CE performances were also conducted at 1 mA cm^{-2} to emphasize the superiority of the Ag@ICOFs decoration layer. It is evident that ICOFs encounter a rapid CE decay with significant cycling fluctuations (98 cycles), while Ag@ICOFs provides a stable plot for almost 340 cycles. The notable lifespan difference demonstrates the enhanced capability of achieving uniform Li deposition/exfoliation and reducing interface residues for Ag@ICOFs. The SEM images in Fig. S10 further show the absence of dendrites on the Ag@ICOFs electrodes after 50 and 100 cycles, indicating the avoidance of concentrated Li deposition and sufficient exfoliation during these operations. In sharp contrast, some irregular dendrites appeared on the ICOF protected Cu electrode (Fig. S11). An optical image of the cycled electrode directly shows that the protective layer is still tightly adhered on Li metal (Fig. S12). In addition, related FT-IR analysis and XRD patterns are also provided in Fig. S13, from which typical characteristic peaks of ICOFs are detected at ~3° (corresponding to the (100) plane) and 1690 cm^{-1} (imine bonds (–C=N–)) respectively. Additionally, the Young's modulus distribution map of the Ag@ICOFs electrode after 100 cycles is provided in Fig. S14, and the measured high modulus value of 6.8 GPa shows that the Ag@ICOFs layer can still suppress dendrites, implying that the layer is stable.

In order to validate the improved effects of Ag@ICOFs in promoting the dispersed distribution of Li ions and stabilizing Li growth, the electrochemical performance of symmetric cells

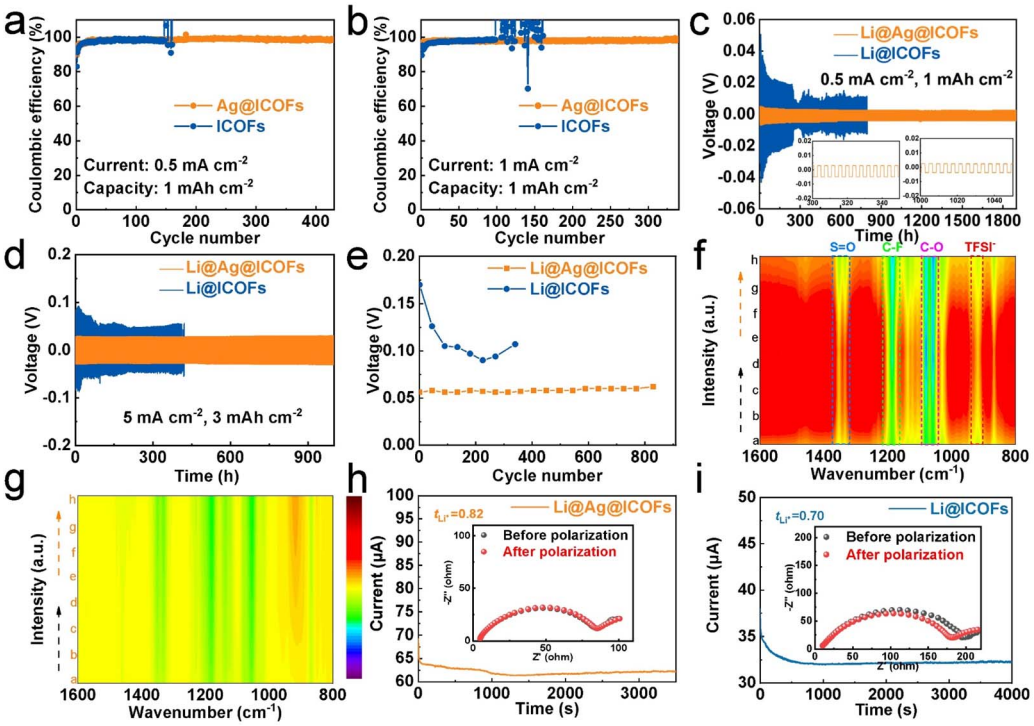

Fig. 5 Coulombic efficiency of the Li anode on the Ag@ICOFs and $ICOF_S$ substrates at (a) 0.5 mA cm^{-2} and (b) 1 mA cm^{-2} at the same capacity of 1 mAh cm^{-2}. Voltage-time profiles of Li@Ag@ICOFs and Li@ICOFs symmetric cells at (c) 0.5 mA cm^{-2} with an areal capacity of 1.0 mAh cm^{-2} and (d) 5.0 mA cm^{-2} with an areal capacity of 3.0 mAh cm^{-2}. (e) Corresponding voltage hysteresis profiles of Ag@ICOFs and ICOFs at a current of 5 mA cm^{-2}. The normalized *in situ* FT-IR transmittance spectra at different stages of (f) Li@ICOFs and (g) Li@Ag@ICOFs electrodes. (h and i) Lithium ion transference numbers of Ag@ICOFs and $ICOF_S$.

using Li@Ag@ICOFs and Li@ICOFs was examined in a range of current densities. Fig. 5c shows that the Li@Ag@ICOFs-based symmetric cell displays a superior lifetime of more than 1900 h (0.5 mA cm^{-2}, 1 mAh cm^{-2}) and a low overpotential of 12.0 mV, extremely longer than that of the cells assembled with ICOF protected electrodes. The described phenomenon would become even more apparent when the current density is increased. Fig. 5d illustrates the obtained results at 5 mA cm^{-2}, from which the symmetric cell with Li@Ag@ICOFs delivers an ultra-stable performance of 1100 h, which far exceeds that of the Li@ICOFs cell (~410 h). A voltage hysteresis comparison of the two symmetric cells is depicted in Fig. 5e, where the low potential hysteresis (~57.2 mV) of the Li@Ag@ICOFs cell can be well maintained, manifesting the stable mass transfer process and uniformly dispersed Li plating/stripping. As depicted in Fig. S15, the Ag@ICOFs-based symmetrical cell exhibits a stable voltage hysteresis when worked at different current densities (1, 2, 3, 5, and 8 mA cm^{-2}), thereby confirming its excellent rate performance. Actually, Li deposition and growth show concentrated and dendritic development at high current densities. Specifically, the presence of Ag nanoparticles enhances electronic conductivity and facilitates electron transport, enabling selective Li deposition in Ag@ICOFs and reducing dendrite generation.

The interface protection layer can avoid the direct contact between the ether-electrolyte and effectively reduce electrolyte consumption due to the SEI formation.[56–58] *In situ* FT-IR measurements were conducted to verify the practical effect of Ag@ICOFs in eliminating the unnecessary electrolyte loss at different deposition/dissolution stages. Remarkably, a continuously decreased FT-IR signal of $TFSI^-$ in the range of 886 cm^{-1} can be observed for the ICOF protected electrode, which can be attributed to $TFSI^-$ decomposition for the breaking of the fragile SEI and additional chemical reactions.[59] Nevertheless, an irreversible increment in the C–O, C–F, and S=O bands at 1079–1057 cm^{-1}, 1184 cm^{-1} and 1332–1353 cm^{-1} also indicates that the ether-based electrolyte undergoes an inevitable depletion (Fig. S16 and **5f**).[60] In comparison, during the whole charge/discharge process, no discernible FT-IR peaks of additional SEI generation are detected for Ag@ICOFs under the same conditions, which means that stable surface passivation on the electrode can be significantly supported by the robust Ag@ICOFs layer (Fig. S17 and **5g**). The ion transference number was also determined for the two decoration layers to study the interface conditions. As displayed in Fig. 5h and i, a larger ion transference number of 0.82 can be obtained using the Ag@ICOFs layer, compared to pristine ICOFs (0.70). The slow ion movement may encounter uneven Li growth and degeneration and then cause the local accumulation and residue of Li metal, easily inducing the breaking of protection layers and fresh SEI production during the continuous Li plating/stripping.[61,62]

To test the viability of the Ag@ICOFs protective layer, full cells were assembled with $LiFePO_4$ as the cathode (Fig. 6a). When tested at a fast-charging current density of 5C (Fig. 6b),

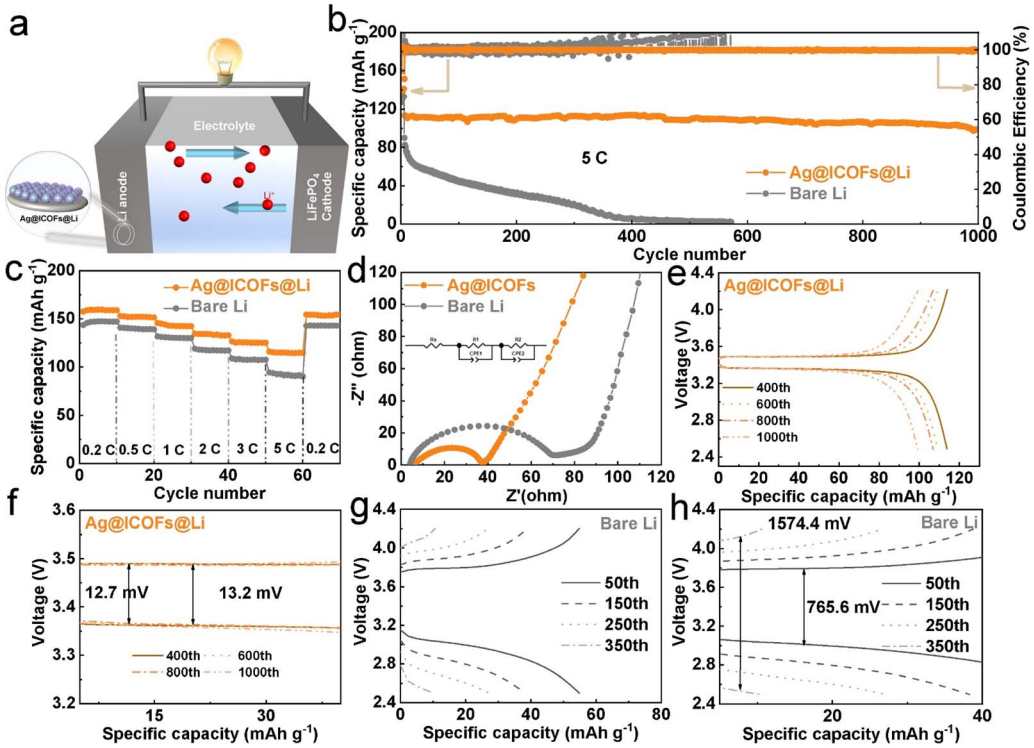

Fig. 6 (a) Schematic diagram of a full battery. Electrochemical performance of Li@Ag@ICOFs|LFP and bare Li|LFP full cells at (b) 5C and (c) different rates. (d) Electrochemical impedance spectra of full cells after 100 cycles. (e) Charge–discharge profiles of Li@Ag@ICOFs|LFP full cells at different cycling numbers and (f) enlarged profiles. (g) Charge–discharge profiles of bare Li|LFP full cells and (h) enlarged profiles.

the full cell using Li@Ag@ICOFs exhibits a stable cycling tendency. In particular, an initial discharge capacity of 113.6 mAh g^{-1} (after the activation of 5 cycles at 1C) with a high CE of 83.4% can be delivered, and then a slight capacity decrease to 99.2 mAh g^{-1} occurs after 1000 cycles, corresponding to a capacity retention of 87.3%. However, for the cell with bare Li, there is a continuous rapid capacity decay and extremely low capacity delivery close to 0 mAh g^{-1} can be noticed after 400 cycles. Similarly, another cathode material (Ni-rich NCM) was also applied to explore the practical utilization of the functional anode. In Fig. S18, the obtained performances of full cells using NCM are provided, from which a high capacity delivery of 147.5 mAh g^{-1} and capacity retention of 84% can be achieved after 50 cycles at 5C, demonstrating the excellent adaptability of NCM and Li@Ag@ICOFs. As demonstrated in Table S1, compared to similar COF materials used in LMBs, Ag@ICOFs shows exceptional electrochemical performances. In addition, as depicted in Fig. 6c, the full cell with Li@Ag@ICOFs demonstrates better rate performances and the advantage of using the Ag@ICOFs layer is particularly evident at a high rate (5C). Moreover, the cell delivers capacities of 159.0 and 115.8 mAh g^{-1} at current densities of 0.2C and 5C, respectively. The electrochemical impedance spectra (EIS) of these two full cells after 200 cycles are shown in Fig. 6d. The interfacial charge transfer resistance of the cell with Li@Ag@ICOFs is determined to be 30.0 Ω, indicating more stable and faster diffusion of ions and electrons compared to another cell (65.7 Ω). Additionally, as exhibited in Fig. 6e, the Li@Ag@ICOFs cell can display a stable voltage plateau and excellent retention during the long-term cycling, incrementally increasing from 12.7 mV in the initial 400th cycle to 13.2 mV in the 1000th cycle (Fig. 6f), which is mainly attributed to the stable interface of the Li@Ag@ICOFs anode that maintains rapid ion diffusion and charge transfer kinetics. On the other hand, as shown in Fig. 6g and h, the voltage polarization of the cell using bare Li dramatically increases from 765.6 mV in the 50th cycle to 1574.4 mV in the 350th cycle. This is possibly due to an excessive build-up of the SEI from unchecked Li dendrites, which obstructs electron transfer and increases charge transfer resistance.

Conclusions

In summary, a functional material of hollow nanospheres assembled from imine-based covalent organic frameworks and built-in Ag sites (Ag@ICOFs) has been constructed and used as an interfacial layer for stabilizing and improving the Li metal anode. Hierarchical lithiophilic sites in Ag@ICOFs (exposed C=N groups and benzene rings and internal Ag nanoparticles) can homogenize the interfacial Li ion flux and induce directional deposition. Specifically, abundant lithiophilic sites in ICOFs play important roles in the first stage of dispersing Li ions and avoiding local concentration, thereby promoting uniform Li distribution. Subsequently, during gradual Li development, Ag sites can guide internal Li injection and inhibit the vertical growth tendency, further inhibiting dendrite formation. The superior capability of promoting dendrite-free

behavior and effectively reducing electrolyte consumption has also been verified using *in situ* optical microscopes and *in situ* FT-IR. As a result, superior electrochemical performances can be achieved, such as a long-term cycling lifespan of 1900 h, high CE values of 99.3% and a low capacity decay of 5.3% after 1000 cycles in a full battery. The artificial SEI of the organic–inorganic composite proposed in this work can provide a new idea for inhibiting Li dendrites.

Author contributions

T. C. Liu and X.-M. Lu performed the chemical research and prepared the manuscript; S. Lu helped with cell assembly and performance testing; C. F. Guo, Z. X. Yu and Y. Wang conceived the idea and designed the research; R. H. Jiang conceived the experimental work and participated in the discussion of the data; M. Guo contributed to the DFT calculations. All authors have given approval to the final version of the manuscript.

Conflicts of interest

The authors declare that they have no known competing financial interests or personal relationships that could have appeared to influence the work reported in this paper.

Data availability

The data supporting this article have been included as part of the SI.

Supplementary information: experimental section, characterization information and electrochemical results. See DOI: https://doi.org/10.1039/d5sc03645c.

Acknowledgements

The authors sincerely thank the Zhejiang Provincial Natural Science Foundation of China (Grant No. LQ23E030016), National Natural Science Foundation of China (52401289) and China Postdoctoral Science Foundation (No. 2023M733154) for their financial support.

Notes and references

1 Y. Liu, X. Tao, Y. Wang, C. Jiang, C. Ma, O. Sheng, G. Lu and X. W. Lou, Self-assembled monolayers direct a LiF-rich interphase toward long-life lithium metal batteries, *Science*, 2022, **375**, 739–745.

2 S. Zhang, R. Li, N. Hu, T. Deng, S. Weng, Z. Wu, D. Lu, H. Zhang, J. Zhang, X. Wang, L. Chen, L. Fan and X. Fan, Tackling realistic Li^+ flux for high-energy lithium metal batteries, *Nat. Commun.*, 2022, **13**, 5431.

3 T. Kang, C. Wang, X. Zhao, Z. Guan, D. Shen, T. Song, Y. Wu, F. Zhang, Y. Tang, Z. Tong and C.-S. Lee, Towards high-rate lithium metal anodes with electrochemically inert and catalytic COF separators, *Energy Storage Mater.*, 2023, **54**, 589–595.

4 J. J. Xu, T. P. Pollard, C. Y. Yang, N. K. Dandu, S. Tan, J. G. Zhou, J. Wang, X. Z. He, X. Y. Zhang, A. M. Li, E. Y. Hu, X. Q. Yang, A. Ngo, O. Borodin and C. S. Wang, Lithium halide cathodes for Li metal batteries, *Joule*, 2023, **7**, 83–94.

5 S. Y. Yao, Y. Yang, Z. W. Liang, J. H. Chen, J. Y. Ding, F. K. Li, J. H. Liu, L. Xi, M. Zhu and J. Liu, A dual-functional cationic covalent organic frameworks modified separator for high energy lithium metal batteries, *Adv. Funct. Mater.*, 2023, **33**, 2212466.

6 P. Molaiyan, M. Abdollahifar, B. Boz, A. Beutl, M. Krammer, N. X. Zhang, A. Tron, M. Romio, M. Ricci, R. Adelung, A. Kwade, U. Lassi and A. Paolella, Optimizing current collector interfaces for efficient "anode-free" lithium metal batteries, *Adv. Funct. Mater.*, 2024, **34**, 2311301.

7 Z. Q. Shi, Y. M. Wang, X. Y. Yue, J. Zhao, M. M. Fang, J. J. Liu, Y. M. Chen, Y. T. Dong, X. Z. Yan and Z. Liang, Mechanically interlocked interphase with energy dissipation and fast Li-ion transport for high-capacity lithium metal batteries, *Adv. Mater.*, 2024, **36**, 202401711.

8 X. B. Cheng, S. J. Yang, Z. C. Liu, J. X. Guo, F. N. Jiang, F. Jiang, X. S. Xiong, W. B. Tang, H. Yuan, J. Q. Huang, Y. P. Wu and Q. Zhang, Electrochemically and thermally stable inorganics-rich solid electrolyte interphase for robust lithium metal batteries, *Adv. Mater.*, 2024, **36**, 202307370.

9 Y. F. Zhu, Z. J. Lao, M. T. Zhang, T. Z. Hou, X. Xiao, Z. H. Piao, G. X. Lu, Z. Y. Han, R. H. Gao, L. Nie, X. R. Wu, Y. Z. Song, C. Y. Ji, J. Wang and G. M. Zhou, A locally solvent-tethered polymer electrolyte for long-life lithium metal batteries, *Nat. Commun.*, 2024, **15**, 3914.

10 Y. X. Yang, C. H. Zhang, G. F. Zhao, Q. An, Z. Y. Mei, Y. J. Sun, Q. J. Xu, X. F. Wang and H. Guo, Regulating the electron structure of covalent organic frameworks by strong electron-withdrawing nitro to construct specific Li^+ oriented channel, *Adv. Energy Mater.*, 2023, **13**, 2300725.

11 Z. Li, Y. Chen, X. Yun, P. Gao, C. Zheng and P. Xiao, Critical review of fluorinated electrolytes for high-performance lithium metal batteries, *Adv. Funct. Mater.*, 2023, **33**, 2300502.

12 H. Wang, Z. Yu, X. Kong, W. Huang, Z. Zhang, D. G. Mackanic, X. Huang, J. Qin, Z. Bao and Y. Cui, Dual-solvent Li-ion solvation enables high-performance Li-metal batteries, *Adv. Mater.*, 2021, **33**, 2008619.

13 L. Dong, Y. Liu, K. Wen, D. Chen, D. Rao, J. Liu, B. Yuan, Y. Dong, Z. Wu, Y. Liang, M. Yang, J. Ma, C. Yang, C. Xia, B. Xia, J. Han, G. Wang, Z. Guo and W. He, High-polarity fluoroalkyl ether electrolyte enables solvation-free Li^+ transfer for high-rate lithium metal batteries, *Adv. Sci.*, 2022, **9**, 2104699.

14 Z. Piao, R. Gao, Y. Liu, G. Zhou and H.-M. Cheng, A review on regulating Li^+ solvation structures in carbonate electrolytes for lithium metal batteries, *Adv. Mater.*, 2023, **35**, 2206009.

15 C.-P. Yang, Y.-X. Yin, S.-F. Zhang, N.-W. Li and Y.-G. Guo, Accommodating lithium into 3D current collectors with a submicron skeleton towards long-life lithium metal anodes, *Nat. Commun.*, 2015, **6**, 8058.

16 L. Deng, L. Dong, Z. Wang, Y. Liu, J. Zhan, S. Wang, K.-P. Song, D. Qi, Y. Sang, H. Liu and H. Chen, Asymmetrically-fluorinated electrolyte molecule design for simultaneous achieving good solvation and high inertness to enable stable lithium metal batteries, *Adv. Energy Mater.*, 2024, **14**, 2303652.

17 Q. Xu, T. Li, Z. Ju, G. Chen, D. Ye, G. I. N. Waterhouse, Y. Lu, X. Lai, G. Zhou, L. Guo, K. Yan, X. Tao, H. Li and Y. Qiu, Li_2ZrF_6-based electrolytes for durable lithium metal batteries, *Nature*, 2025, **637**, 339–346.

18 L. Qian, H. Zhu, T. Qin, R. Yao, J. Zhao, F. Kang and C. Yang, Ultralow-salt-concentration electrolyte for high-voltage aqueous Zn metal batteries, *Adv. Funct. Mater.*, 2023, **33**, 2301118.

19 Q. Meng, M. Fan, X. Chang, H. Li, W.-P. Wang, Y.-H. Zhu, J. Wan, Y. Zhao, F. Wang, R. Wen, S. Xin and Y.-G. Guo, A functional prelithiation separator promises sustainable high-energy lithium-ion batteries, *Adv. Energy Mater.*, 2023, **13**, 2300507.

20 X. Fan, Y. Zhang, Y. Dou, X. Li, Z. Zhao, X. Zhang, H. Wu and S. Qiao, Covalent organic framework fiber-constructed artificial solid electrolyte interphase layer: facilitated uniform deposition of Li^+ and encapsulated Li dendrite, *ACS Appl. Mater. Interfaces*, 2023, **15**, 51694–51703.

21 L. Zheng, R. Lv, C. Luo, Y. Guo, M. Yang, K. Hu, K. Wang, L. Li, F. Wu and R. Chen, Amorphous high-entropy alloy interphase for stable lithium metal batteries, *Adv. Energy Mater.*, 2024, **14**, 2402042.

22 D. Park and D.-W. Kim, In-vitro alloyable unidimensional polymeric interface to mitigate pulverization and dendritic growth for long lifespan lithium metal batteries, *Adv. Energy Mater.*, 2025, **15**, 2403525.

23 J. Kriegler, H. Ballmes, S. Dib, A. G. Demir, L. Hille, Y. Liang, L. Wach, S. Weinmann, J. Keilhofer, K. J. Kim, J. L. M. Rupp and M. F. Zaeh, Surface reconditioning of lithium metal electrodes by laser treatment for the industrial production of enhanced lithium metal batteries, *Adv. Funct. Mater.*, 2024, **34**, 2313766.

24 Y. Fan, D. Kim, Y. Chen, D. Bi, Q. Han, Q. Cai, X. Hu, S. Mateti, B. Yu and Y. I. Chen, Nitrogen-doped anodic Li oxide films as robust Li metal anodes and solid-state electrolytes, *Adv. Energy Mater.*, 2024, **14**, 2400933.

25 M. Gong, R. Yu, C. Zhou, Y. Yu, Q. Pan, C. Dong, C. Shen, Y. Guan, C. Sun, L. Mai and X. Xu, Mechanically robust current collector with gradient lithiophilicity induced by spontaneous lithium ion diffusion for stable lean-lithium metal batteries, *ACS Nano*, 2024, **18**, 20648–20658.

26 S. Yu, X. Yu, S. Shivakumar, S. Wang, E. Qiu, Q. Miao, J. Gao, M. Wei, J. Zhou, Z. Chen and P. Liu, Defect-mediated faceted lithium nucleation on carbon composite substrates, *ACS Nano*, 2024, **18**, 17031–17040.

27 M. Yang, K. Yang, Y. Wu, Z. Wang, T. Ma, D. Wu, L. Yang, J. Xu, P. Lu, J. Peng, Z. Jiang, X. Zhu, Q. Gao, F. Xu, L. Chen, H. Li and F. Wu, Dendrite-free all-solid-state lithium metal batteries by in situ phase transformation of the soft carbon–Li_3N interface layer, *ACS Nano*, 2024, **18**, 16842–16852.

28 Z. H. Wu, C. Y. Wang, Z. Y. Hui, H. D. Liu, S. Wang, S. C. Yu, X. Xing, J. Holoubek, Q. S. Miao, H. L. Xin and P. Liu, Growing single-crystalline seeds on lithiophobic substrates to enable fast-charging lithium-metal batteries, *Nat. Energy*, 2023, **8**, 340–350.

29 J. Zhan, L. Deng, Y. Liu, M. Hao, Z. Wang, L.-T. Dong, Y. Yang, K. Song, D. Qi, J. Wang, S. Wang, H. Liu, W. Zhou and H. Chen, Self-Selective (220) Directional Grown Copper Current Collector Design for Cycling-Stable Anode-Less Lithium Metal Batteries, *Adv. Mater.*, 2025, **37**, 2413420.

30 K. Yan, Z. D. Lu, H. W. Lee, F. Xiong, P. C. Hsu, Y. Z. Li, J. Zhao, S. Chu and Y. Cui, Selective deposition and stable encapsulation of lithium through heterogeneous seeded growth, *Nat. Energy*, 2016, **1**, 16010.

31 D. Spencer-Jolly, V. Agarwal, C. Doerrer, B. K. Hu, S. M. Zhang, D. L. R. Melvin, H. Gao, X. W. Gao, P. Adamson, O. Magdysyuk, P. S. Grant, R. A. House and P. G. Bruce, Structural changes in the silver-carbon composite anode interlayer of solid-state batteries, *Joule*, 2023, **7**, 503–514.

32 Y. J. Fang, S. L. Zhang, Z. P. Wu, D. Y. Luan and X. W. Lou, A highly stable lithium metal anode enabled by Ag nanoparticle-embedded nitrogen-doped carbon macroporous fibers, *Sci. Adv.*, 2021, **7**, eabg3626.

33 P. Zhao, Y. Zhang, B. Sun, R. Qiao, C. Li, P. Hai, Y. Wang, F. Liu and J. Song, Enhancing anion-selective catalysis for stable lithium metal pouch cells through charge separated COF interlayer, *Angew. Chem., Int. Ed.*, 2024, **63**, e202317016.

34 J. Xue, Z. Sun, B. Sun, C. Zhao, Y. Yang, F. Huo, A. Cabot, H. K. Liu and S. Dou, Covalent organic framework-based materials for advanced lithium metal batteries, *ACS Nano*, 2024, **18**, 17439–17468.

35 S. Zheng, Y. Fu, S. Bi, X. Yang, X. Xu, X. Li, Q. Xu and G. Zeng, Three-dimensional covalent organic framework with dense lithiophilic sites as protective layer to enable high-performance lithium metal battery, *Angew. Chem., Int. Ed.*, 2025, **64**, e202417973.

36 D. Chen, S. Huang, L. Zhong, S. Wang, M. Xiao, D. Han and Y. Meng, In Situ Preparation of Thin and Rigid COF Film on Li Anode as Artificial Solid Electrolyte Interphase Layer Resisting Li Dendrite Puncture, *Adv. Funct. Mater.*, 2020, **30**, 1907717.

37 X. Pang, B. Shi, Y. Liu, Y. Li, Y. Zhang, T. Wang, S. Xu, X. Wang, Z. Liu, N. Xing, X. Liang, Z. Zhu, C. Fan, Y. Liu, H. Wu and Z. Jiang, Phosphorylated Covalent Organic Framework Membranes Toward Ultrafast Single Lithium-Ion Transport, *Adv. Mater.*, 2024, **36**, 2413022.

38 A. P. Côté, A. I. Benin, N. W. Ockwig, M. O'Keeffe, A. J. Matzger and O. M. Yaghi, Porous, crystalline, covalent organic frameworks, *Science*, 2005, **310**, 1166–1170.

39 Y. T. Li, J. Duan, Y. Z. Wang, L. K. Teng, H. Liu, J. Q. Li, M. Q. Liu, W. S. He, H. W. Hu, L. L. Wang, W. Lyu and Y. Z. Liao, Cu-mediated bipolar-type extended π-conjugated microporous polymers for lithium-ion battery cathodes with high energy density and fast-charging capability, *Chem. Sci.*, 2025, **16**, 11311–11321.

40 Y. An, S. Tan, Y. Liu, K. Zhu, L. Hu, Y. Rong and Q. An, Designs and applications of multi-functional covalent organic frameworks in rechargeable batteries, *Energy Storage Mater.*, 2021, **41**, 354–379.
41 S. A. Ahmed, Q.-B. Liao, Q. Shen, M. M. F. Ashraf Baig, J. Zhou, C.-F. Shi, P. Muhammad, S. Hanif, K. Xi, X.-H. Xia and K. Wang, pH-dependent slipping and exfoliation of layered covalent organic framework, *Chem.–Eur. J.*, 2020, **26**, 12996–13001.
42 X.-M. Lu, T. Liu, Y. Wang and F.-H. Du, Inside-outside lithium deposition achieved by the unusual strategy of constructing the hierarchical lithiophilicity for dendrite-free and durable lithium metal anode, *Batteries Supercaps*, 2022, **5**, e202200114.
43 M. Matsumoto, R. R. Dasari, W. Ji, C. H. Feriante, T. C. Parker, S. R. Marder and W. R. Dichtel, Rapid, Low temperature formation of imine-linked covalent organic frameworks catalyzed by metal triflates, *J. Am. Chem. Soc.*, 2017, **139**, 4999–5002.
44 S. Li, S. Xu, E. Lin, T. Wang, H. Yang, J. Han, Y. Zhao, Q. Xue, P. Samorì, Z. Zhang and T. Zhang, Synthesis of single-crystalline sp2-carbon-linked covalent organic frameworks through imine-to-olefin transformation, *Nat. Chem.*, 2025, **17**, 226–232.
45 A. Tosello Gardini, U. Raucci and M. Parrinello, Machine learning-driven molecular dynamics unveils a bulk phase transformation driving ammonia synthesis on barium hydride, *Nat. Commun.*, 2025, **16**, 2475.
46 X. Tang, L.-P. Lv, S. Chen, W. Sun and Y. Wang, Tin-nitrogen coordination boosted lithium-storage sites and electrochemical properties in covalent-organic framework with layer-assembled hollow structure, *J. Colloid Interface Sci.*, 2022, **622**, 591–601.
47 Z. Lei, Q. Yang, Y. Xu, S. Guo, W. Sun, H. Liu, L.-P. Lv, Y. Zhang and Y. Wang, Boosting lithium storage in covalent organic framework via activation of 14-electron redox chemistry, *Nat. Commun.*, 2018, **9**, 576.
48 H. L. Meng, S. Y. Lin, J. J. Feng, L. Zhang and A. J. Wang, Coordination regulated pyrolysis synthesis of ultrafine FeNi/$(FeNi)_9S_8$ nanoclusters/nitrogen, sulfur-codoped graphitic carbon nanosheets as efficient bifunctional oxygen electrocatalysts, *J. Colloid Interface Sci.*, 2022, **610**, 573–582.
49 Q.-D. Ruan, L. Zhang, J.-J. Feng, L.-X. You, Z.-G. Wang and A.-J. Wang, Three-dimensional self-supporting superstructured double-sided nanoneedles arrays of iron carbide nanoclusters embedded in manganese, nitrogen co-doped carbon for highly efficient oxygen reduction reaction, *J. Colloid Interface Sci.*, 2022, **614**, 655–665.
50 W. Sun, X. Tang, Q. Yang, Y. Xu, F. Wu, S. Guo, Y. Zhang, M. Wu and Y. Wang, Coordination-induced interlinked covalent- and metal–organic-framework hybrids for enhanced lithium storage, *Adv. Mater.*, 2019, **31**, 1903176.
51 Y. J. Wu, Y. S. Liu, C. Y. Hsieh, P. M. Lee, Y. S. Wei, C. H. Liao and C. Y. Liu, Study of p-type AlN-doped SnO_2 thin films and its transparent devices, *Appl. Surf. Sci.*, 2015, **328**, 262–268.
52 I. Bertóti, Characterization of nitride coatings by XPS, *Surf. Coat. Technol.*, 2002, **151–152**, 194–203.
53 Y. J. Fang, S. L. Zhang, Z. P. Wu, D. Y. Luan and X. W. Lou, A highly stable lithium metal anode enabled by Ag nanoparticle-embedded nitrogen-doped carbon macroporous fibers, *Sci. Adv.*, 2021, **7**, eabg3626.
54 Z. Peng, J. Song, L. Huai, H. Jia, B. Xiao, L. Zou, G. Zhu, A. Martinez, S. Roy, V. Murugesan, H. Lee, X. Ren, Q. Li, B. Liu, X. Li, D. Wang, W. Xu and J.-G. Zhang, Enhanced stability of Li metal anodes by synergetic control of nucleation and the solid electrolyte interphase, *Adv. Energy Mater.*, 2019, **9**, 1901764.
55 J. Xiao, Q. Li, Y. Bi, M. Cai, B. Dunn, T. Glossmann, J. Liu, T. Osaka, R. Sugiura, B. Wu, J. Yang, J.-G. Zhang and M. S. Whittingham, Understanding and applying coulombic efficiency in lithium metal batteries, *Nat. Energy*, 2020, **5**, 561–568.
56 H. S. Wang, Y. Y. Liu, Y. Z. Li and Y. Cui, Lithium metal anode materials design: interphase and host, *Electrochem. Energy Rev.*, 2019, **2**, 509–517.
57 W. Ye, F. Pei, X. Lan, Y. Cheng, X. Fang, Q. Zhang, N. Zheng, D.-L. Peng and M.-S. Wang, Stable nano-encapsulation of lithium through seed-free selective deposition for high-performance Li battery anodes, *Adv. Energy Mater.*, 2020, **10**, 1902956.
58 K. Yan, Z. Lu, H.-W. Lee, F. Xiong, P.-C. Hsu, Y. Li, J. Zhao, S. Chu and Y. Cui, Selective deposition and stable encapsulation of lithium through heterogeneous seeded growth, *Nat. Energy*, 2016, **1**, 16010.
59 T. Liu, J. Ge, Y. Xu, L.-P. Lv, W. Sun and Y. Wang, Organic supramolecular protective layer with rearranged and defensive Li deposition for stable and dendrite-free lithium metal anode, *Energy Storage Mater.*, 2020, **32**, 261–271.
60 X.-M. Lu, Y. Cao, Y. Sun, H. Wang, W. Sun, Y. Xu, Y. Wu, C. Yang and Y. Wang, sp-carbon-conjugated organic polymer as multifunctional interfacial layers for ultra-long dendrite-free lithium metal batteries, *Angew. Chem., Int. Ed.*, 2024, **63**, e202320259.
61 M. Cui, N. Gao, W. Zhao, H. Zhao, Z. Cao, Y. Qin, G. Gao, K. Xi, Y. Su and S. Ding, Self-regulating interfacial space charge through polyanion repulsion effect towards dendrite-free polymer lithium-metal batteries, *Adv. Energy Mater.*, 2024, **14**, 2303834.
62 X.-M. Lu, H. Wang, Y. Sun, Y. Xu, W. Sun, Y. Wu, Y. Zhang, C. Yang and Y. Wang, Covalent triazine based frameworks with donor-donor-π-acceptor structures for dendrite-free lithium metal batteries, *Angew. Chem., Int. Ed.*, 2024, **63**, e202409436.